*Earth Planets Space*, **51**, 233–246, 1999

# Fine structure of aftershock distribution of the 1997 Northwestern Kagoshima Earthquakes with a three-dimensional velocity model

Hiroki Miyamachi, Kazuhiro Iwakiri, Hiroshi Yakiwara, Kazuhiko Goto, and Toshiki Kakuta

*Faculty of Science, Kagoshima University, Kagoshima 890-0065, Japan*

(Received September 4, 1998; Revised February 6, 1999; Accepted February 6, 1999)

In 1997, two earthquakes (M6.5 and M6.3) occurred in the northwestern part of Kagoshima Prefecture, Japan. We carried out temporary seismic observation to obtain the detailed aftershock distribution. We constructed a 3-D P wave velocity model by inverting the travel times of aftershocks observed at 14 seismic stations in and around the focal area and relocated more than 14,000 aftershocks with the 3-D velocity model.

The general features of the aftershock distribution are as follows: (1) Aftershocks of the first main shock (M6.5) are distributed with a strike of nearly E-W (N100°E) in a vertical plane with a horizontal length of 21 km and a depth range of 2 to 9 km; (2) The second main shock (M6.3) has an 'L'-shaped aftershock distribution: one plane strikes nearly E-W, which is parallel to the aftershock zone of the first main shock, and the other is a conjugate plane; (3) An obvious seismicity gap of about 3 km wide is found between the aftershock zones striking E-W for the first and second main shocks; (4) The aftershock activities are generally low around the hypocenters of the two main shocks.

Our results show that most of aftershocks occurred not in high or low velocity zones, but in intermediate velocity areas. Several vertical linear distributions of aftershocks are also confirmed in the two focal zones striking E-W. These peculiar distributions suggest that the aftershock activity is affected by the underground structural boundaries.

## 1. Introduction

Two strong shallow earthquakes occurred at about 7.5 km depth beneath Mt. Shibi in the northwestern part of Kagoshima Prefecture, Japan, on March 26 and May 13, 1997, as shown in Fig. 1. More than fourteen thousands of aftershocks were recorded following the two main shocks (Kakuta *et al.*, 1998). Miyamachi *et al.* (1998) carried out a temporary seismic observation by installing 12 portable stations in and around the aftershock region. They found that the first main shock (M6.5) was followed by aftershocks distributed in an area of about 20 km long by 2 km wide with a strike of nearly E-W (N100°E), while the aftershocks of the second shock are distributed in an 'L'-shaped area composed of two planes striking E-W and N-S. Focal depths ranged from 0 to 10 km for the aftershocks of the first shock and from 0 to 8 km for those of the second shock. The horizontal distance between the epicenters of the two shocks is only 5 km. The focal zones of the two shocks are, however, obviously different from each other. Kakuta *et al.* (1998) also reported a fault mechanism of a left-lateral strike-slip fault trending E-W for the first shock.

Geological studies of the aftershock region found a complicated surface geology including a large horizontal bending structure of the Shimanto Supergroup and an intrusion of granite (Murata, 1987; Yoneda and Iwamatsu, 1987). Therefore, it is reasonably expected that the lateral seismic velocity variation is large in the region. To reveal a fine spatial distribution of the aftershocks in such a complicated region, an accurate velocity structure, namely three-dimensional velocity structure, must be applied for the hypocenter determination. For example, Miyamachi and Moriya (1987) and Hirahara *et al.* (1992) obtained precise aftershock distributions of the 1982 Urakawa-Oki Earthquake (M6.8) and the 1984 Western Nagano Prefecture Earthquake (M6.8) on the basis of three-dimensional velocity structure, respectively. Recently, Zhao and Negishi (1998) revealed the detailed 3-D P and S wave velocity structure of the 1995 Kobe Earthquake (M7.2) focal zone. They pointed out that areas with high aftershock activity are generally associated with low Poisson's ratio and the main shock is located in a zone with low P and S wave velocities and a high Poisson's ratio. In this manner, a seismic tomography of a focal zone can be expected to give a new insight of the seismic velocity structure, the aftershock distribution and the rupture process of the main shock.

The main purpose of the present study is to obtain a precise aftershock distribution for a better understanding of the two strong earthquakes in northwest Kagoshima. We have estimated the three-dimensional velocity structure in the focal areas and relocated the aftershocks with the obtained 3-D structure. We also investigated the relations of the obtained velocity structure to the aftershock distribution, surface geology and Bouguer gravity anomaly in the study area. However, our main interest in this study is on the aftershock activity during the period of the temporary seismic observation.

## 2. Method

Our analysis proceeds in the following way; at first, we estimated a one-dimensional (1-D) velocity structure model by using the simultaneous inverse method of Crosson (1976). The 1-D structure is adopted as an initial velocity model for the three-dimensional (3-D) inversion. Next, in order

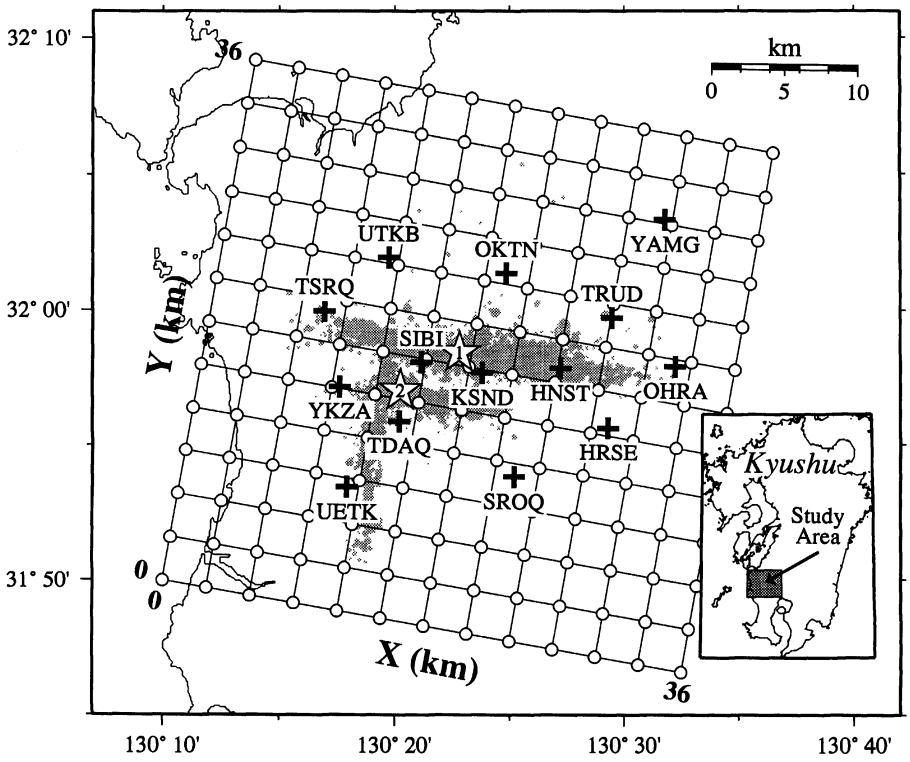


Fig. 1. Map showing the seismic station locations (crosses) with station codes used in the present study. The stations SIBI and YAMG are the telemetered seismic stations of Nansei-Toko Observatory for Earthquakes and Volcanoes, Kagoshima University (NOEV), others are the temporary stations. Two stars numbered indicate the main shock locations occurred on March 26 (M6.5, number 1) and May 13 (M6.3, number 2), 1997, respectively. The shaded area corresponds to the aftershock distribution accompanied with the main shocks. In the figure, the Cartesian coordinate system with the grid nodes (open circles) used in the three-dimensional inversion is also described.

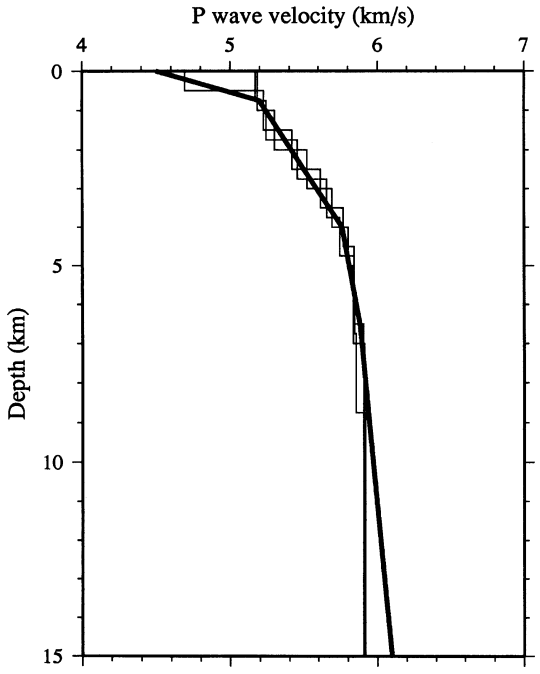


Fig. 2. One-dimensional P wave velocity model estimated by the inversion. Thin lines indicate the results of each inversion. Thick line is the final velocity model which is applied to the initial hypocenter determination.

Table 1. Station corrections at each station obtained by the inversions. The station correction at HNST is fixed to be 0.0 sec during the inversion.

| Station code | Height (meters) | 1-D Inversion (seconds) | 3-D Inversion (seconds) |
|---|---|---|---|
| YKZA | 250 | 0.05 | 0.04 |
| TDAQ | 280 | 0.04 | 0.01 |
| OHRA | 240 | 0.05 | 0.04 |
| HRSE | 170 | 0.13 | 0.15 |
| OKTN | 200 | 0.04 | 0.01 |
| SROQ | 100 | 0.00 | 0.02 |
| TRUD | 170 | −0.08 | −0.08 |
| TSRQ | 160 | 0.09 | 0.10 |
| UTKB | 240 | 0.08 | 0.10 |
| UETK | 60 | −0.05 | −0.03 |
| KSND | 300 | 0.07 | 0.03 |
| HNST | 150 | 0.00* | 0.00* |
| SIBI | 659 | 0.14 | 0.02 |
| YMAG | 400 | −0.01 | −0.03 |

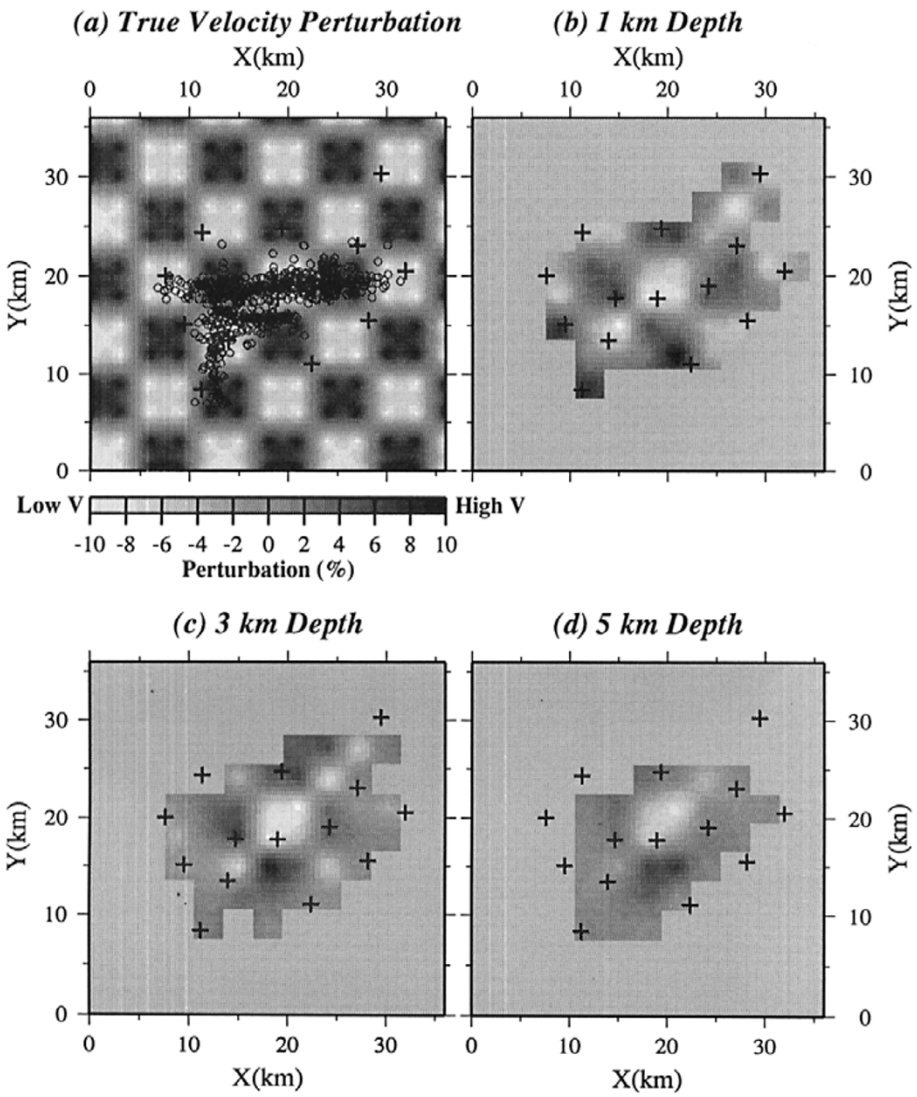


Fig. 3. The checker-board resolution test. The artificial velocity model and the initial epicenters (open circles) are presented in (a). Results of the test are shown in (b)–(d) for 1 km, 3 km and 5 km depths. Crosses indicate the station locations.

to obtain the 3-D velocity model, the simultaneous inverse method of Thurber (1983) was applied to P wave travel time data of the aftershocks. In this method, the model space is represented by a number of three-dimensional grid nodes, and the velocity at each grid node is estimated by inverting the travel times. The velocity at any point in the model space is linearly interpolated from the velocities at 8 grid nodes surrounding that point. Travel times and ray paths are determined with the pseudo-bending method of Um and Thurber (1987). Reliability of the solutions obtained by the 3-D inversion is inspected with the checker-board resolution test (Humphreys and Clayton, 1988; Inoue *et al.*, 1990).

## 3. Seismic Observation and Data

During a period from March 28, two days after the first main shock, to June 19, 1997, we carried out a temporary seismic observation by setting up 12 portable seismic stations, as shown in Fig. 1. At each station, one vertical seismometer and a portable event-triggered recording system were installed. The time calibration of the system was carried out automatically by GPS at every 4 hours. Seismic waves were digitally recorded with a frequency of 100 Hz and stored in a 20 MB memory board. It should be noted that the observation was interrupted sometimes because of the small memory storage. For details of the observation, see Miyamachi *et al.* (1998). We also used the data from two permanent seismic stations, which belong to the Nansei-Toko Observatory for Earthquakes and Volcanoes, Kagoshima University (NOEV) and are located in the present study area. The total number of seismic stations is 14. In the present study, only P wave arrival time data are used and their uncertainties (reading errors) are usually less than 0.05 sec. During the period of the temporary seismic observation, we have detected more than 14,000 aftershocks recorded at more than 10 stations.

## 4. One-Dimensional Velocity Inversion

To have an initial velocity model for the 3-D inversion, we estimated a 1-D P wave velocity model together with station corrections and hypocenters by using the method of Crosson (1976). Because the horizontally homogeneous layered ve-

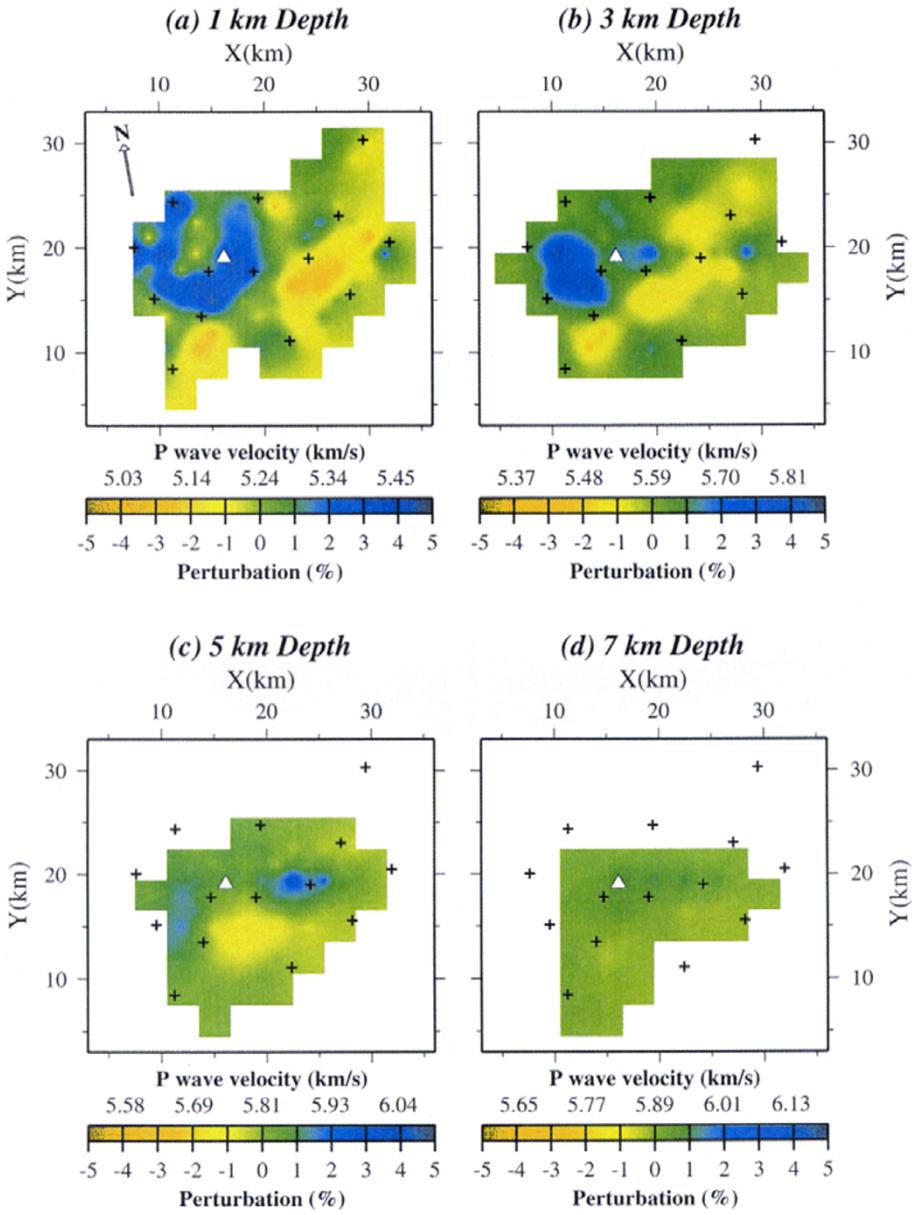


Fig. 4. P wave velocity distributions at depths of 1 km, 3 km, 5 km, and 7 km, estimated by the 3-D inversion. The triangle corresponds to Mt. Shibi. Crosses are the station locations.

locity structure is assumed in the method, we performed the inversions with various thickness of the layers as the respective starting models. We used 14 seismic stations and selected 613 aftershocks shallower than 10 km; they have a uniform distribution in the study area. As a result, the total number of P wave arrival times is 7,717. The standard deviation of the travel time residuals is generally reduced to 0.05 sec in the final model after 4 iterations against 0.11 sec in the starting model. The diagonal elements of the resolution matrix for the velocities estimated are usually greater than 0.9, and the standard errors are less than 0.02 km/s. We compiled the results of all inversions and constructed the final 1-D velocity model as shown in Fig. 2. The averaged station corrections obtained by the inversions are shown in Table 1.

## 5. Three-Dimensional Velocity Inversion

We relocated all the aftershocks, which were recorded during the temporary seismic observation, with the 1-D velocity model and station corrections using the method of Hirata and Matsu'ura (1987). Then we selected 628 aftershocks well located in the study area for the 3-D velocity inversion. The epicenters are shown in Fig. 3. The total number of P wave arrival times is 7,895. In the study area we set up 13 grid nodes with an interval of 3 km along the $X$-axis directed to N100°E, and 13 grid nodes along the $Y$-axis at the same interval. On the $Z$-axis, 7 grid nodes are set up at depths of $-5$, 1, 3, 5, 7, 9 and 15 km. According to the results of the 1-D inversion, initial velocities at the grid points along the $Z$-axis are assigned to be 2.0, 5.24, 5.59, 5.81, 5.89, 5.94 and 6.1 km/s, respectively. The initial station corrections are the same as those of the results of the 1-D inversion.

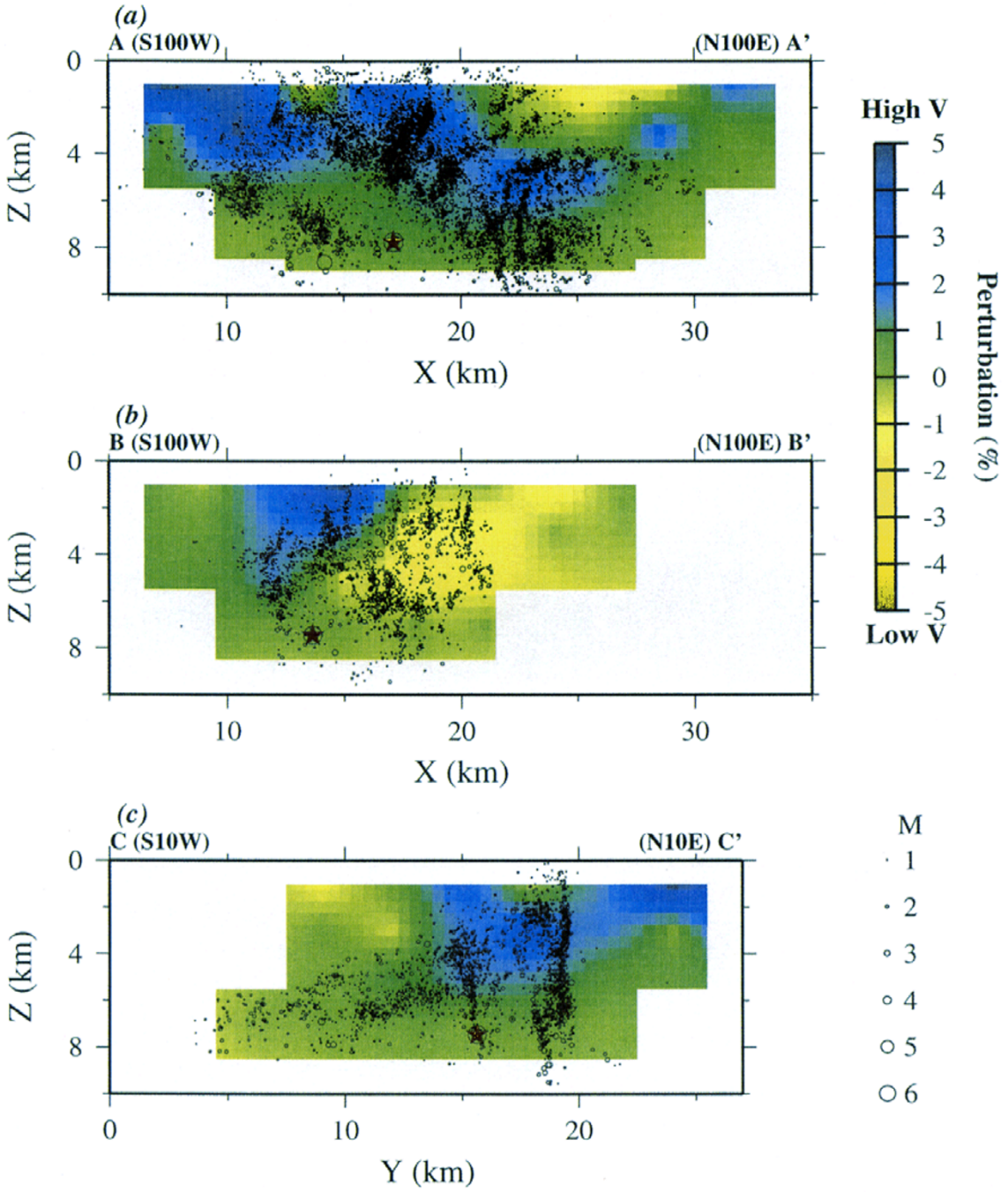


Fig. 5. P wave velocity distributions projected on the vertical sections along the lines shown in Fig. 7 : (a) A–A', (b) B–B' and (c) C–C'. Aftershocks (circles) enclosed in each box in Fig. 7 are also plotted. The red star in (a) indicates the first main shock and those in (b) and (c) the second main shock.

Before applying the 3-D inverse method to the real data, we carried out the checker-board resolution test presented by Humphreys and Clayton (1988) and Inoue *et al.* (1990) to examine the reliability of the inversion. We generated an artificial travel time data set for the real hypocenter and station distributions, and applied the inverse method to the data set. In the artificial velocity model, we assigned ±10% velocity perturbations alternately to every 2 grid nodes in each layer. The result is shown in Fig. 3. Because of the small number of stations and spatially non-uniform distribution of the aftershocks, P wave perturbations are resolved only in the central small area at depths of 1, 3 and 5 km. We also found that the estimated velocity perturbations are somewhat smaller than true values. Though the resolution is not sufficient, it is found that the relative relationship of the velocity distribution, namely high or low velocity zones, is preserved in the shallow layers. Solutions at depths 7 and 9 km are less reliable because few events exist at those depths.

In the 3-D inversion, the standard deviation of the travel time residuals in the initial model is 0.05 sec, and after 6 iterations it decreases to 0.03 sec. The inverted P wave velocity distributions are presented in Fig. 4. At 1 km depth, the high velocities of 5.3 to 5.4 km/s are distributed in a 'U'-shaped zone including Mt. Shibi in the northwestern part of the re-

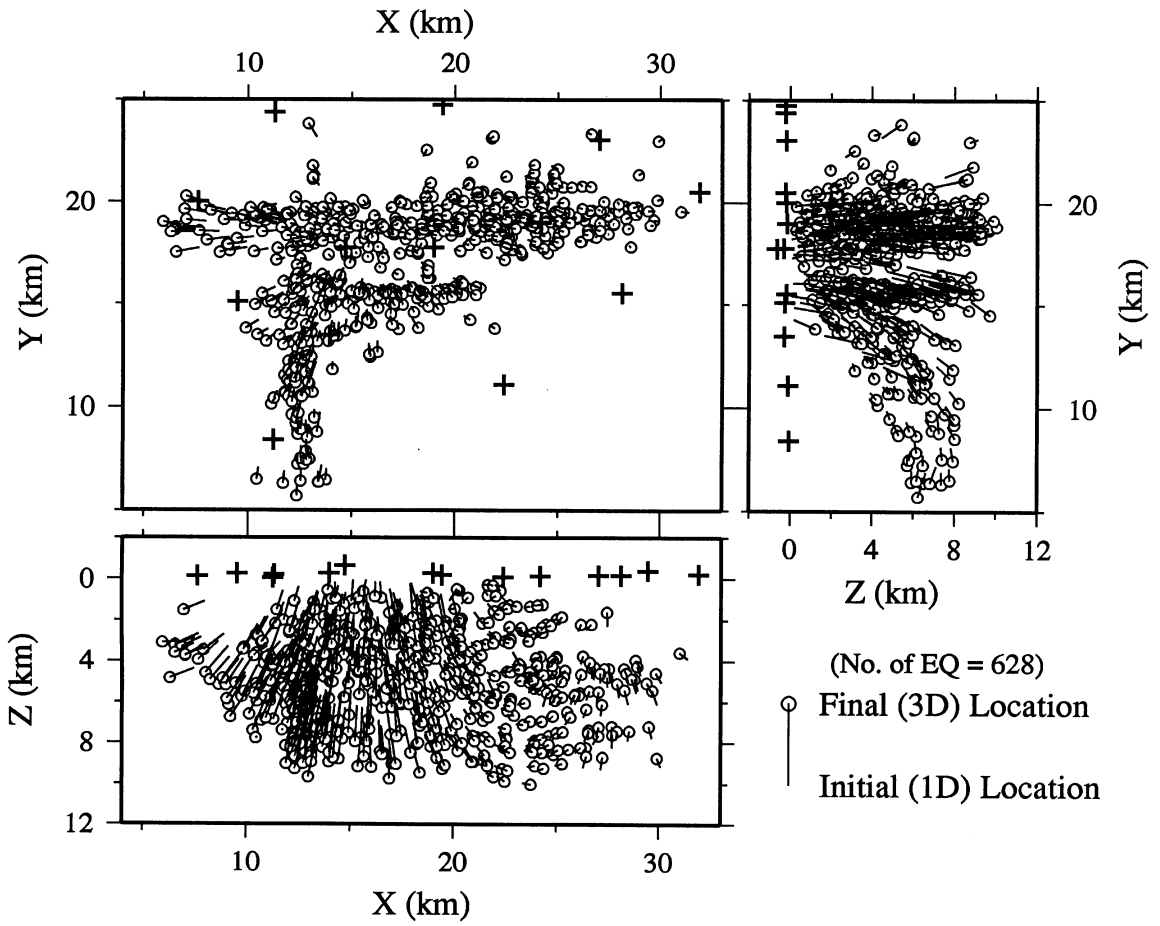


Fig. 6. Relation between the initial (1-D) and final (3-D) locations of aftershocks. Crosses are the station locations.

solved area, while low velocities of 5.1 km/s are located in the areas to the east and south of Mt. Shibi. At 3 km depth, we find a high velocity zone of 5.7 to 5.8 km/s to the west of Mt. Shibi and a low velocity zone of 5.5 km/s occupying the southeastern half of the resolved area. Velocity perturbations are less significant at 5 km depth and less reliable in the layers deeper than 7 km as shown by the checker-board test. The station corrections obtained are listed in Table 1. The 3-D station correction at SIBI, which is the highest station among those used in the present analysis, is largely different from the 1-D one, because station heights are not taken into consideration in the 1-D inversion.

Figure 5 shows the velocity perturbations along vertical cross sections which locations are shown in Fig. 7. Aftershocks in each box in Fig. 7 are also plotted in Fig. 5. Two high velocity zones dominate in the A–A' section striking nearly E-W (Fig. 5(a)): one is zones in the western shallow area ($X = 7$ to 12 km) , the other is gradually inclined to the east at depths of 1 to 6 km in the central area ($X = 15$ to 25 km). We can also find a small area of low velocity at $X = 13$ to 14 km. In addition, a low velocity zone spreads in the middle to eastern shallow areas. Figure 5(b) indicates a distinguishable velocity contrast near the middle part: a high velocity zone is in a shallower part at $X = 12$ to 16 km and it contacts obliquely with a low velocity zone of 2 to 6 km deep in the eastern side. In the N-S section (Fig. 5(c)), a high velocity zone is limited in the northern area. Thus, the study area is characterized by the large lateral velocity variation.

Figure 6 presents the relations between the initial hypocenters (1-D) and the final ones (3-D) obtained by the inversion. The 3-D hypocenters are generally deeper and more distant from Mt. Shibi than the 1-D ones except those in the easternmost area: the differences is larger than 3 km in focal depth and usually less than 1 km in epicenter. These differences between the 3-D and 1-D locations around Mt. Shibi are probably due to the high velocity zones just beneath Mt. Shibi: namely, velocities in the shallow area range from 4.5 to 5.6 km/s in the 1-D model (Fig. 2), while they are 5.4 to 5.8 km/s in the 3-D model.

## 6. Aftershock Distribution with the 3-D Velocity Model

In order to relocate aftershocks, we performed an additional 3-D velocity inversion, shifting grid points by a half grid interval size (1.5 km) in the $X$ and $Y$ directions, and construct a 3-D velocity model by compiling the results. We determined hypocenters of the second main shock (M6.3) as well as more than 14,000 aftershocks observed during the temporary seismic observation with the 3-D model, as shown in Fig. 7. The standard errors of the hypocentral locations are usually less than $\pm 0.14$ km for epicenters and $\pm 0.2$ km for focal depths.

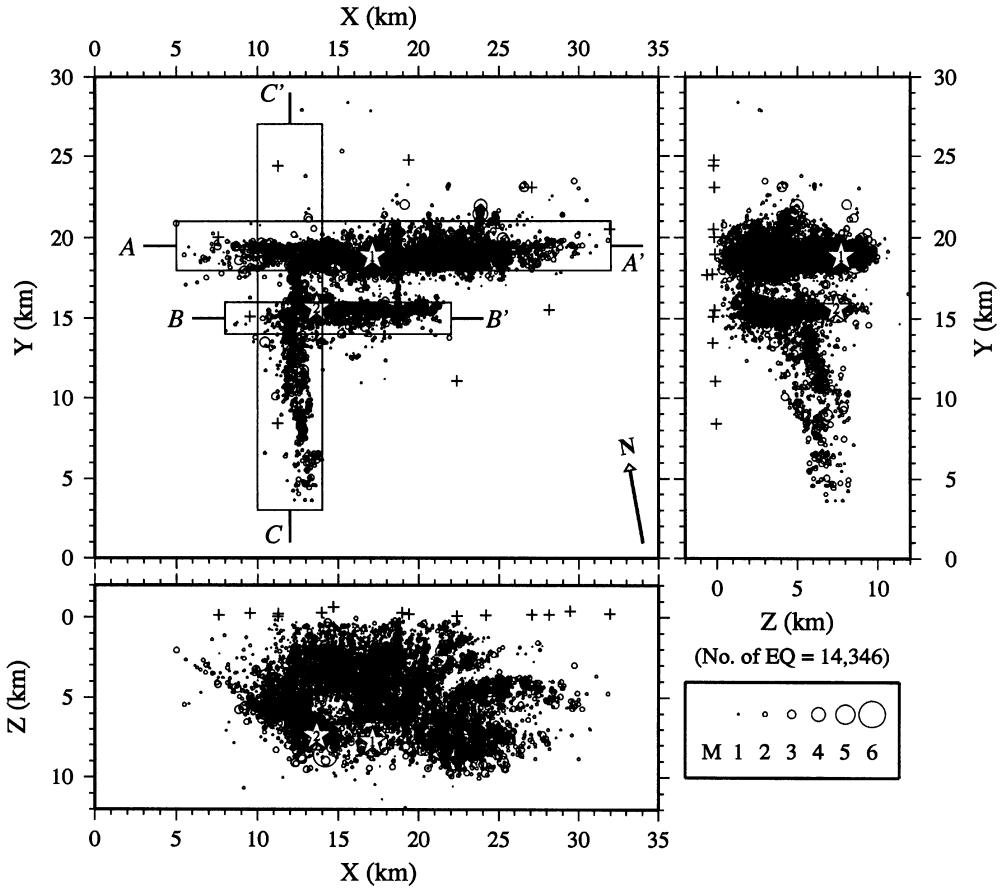


Fig. 7. Aftershock distribution during March 29 to June 19, 1997, obtained by the hypocenter determination for the 3-D velocity model. Two stars indicate the first and second main shock locations, respectively. Thick lines, A–A', B–B' and C–C' are the locations of the vertical sections in Fig. 5 and aftershocks in each box are plotted in the sections.

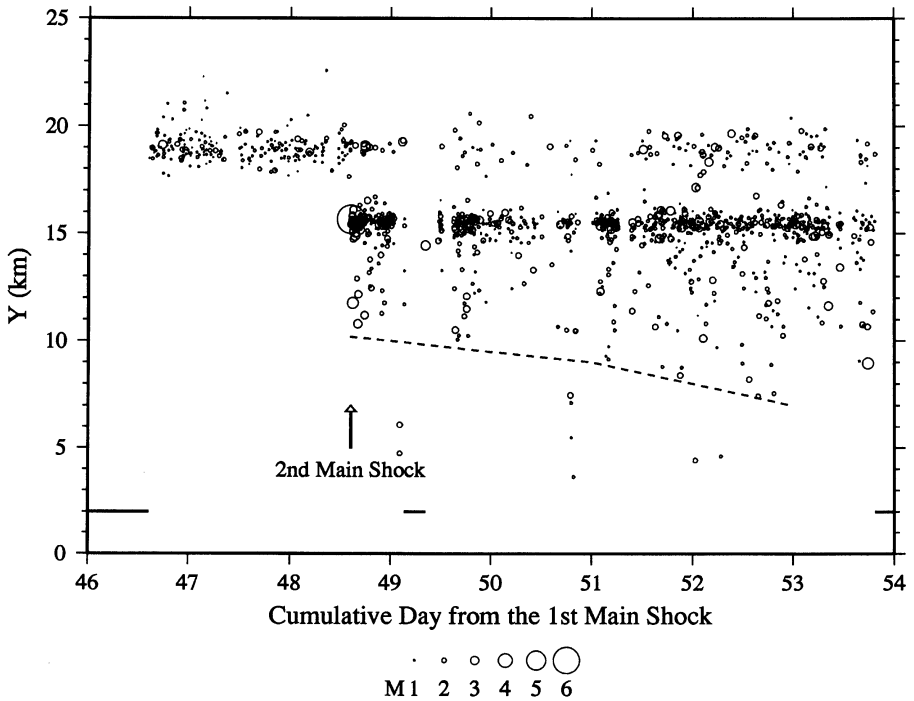


Fig. 8. A diagram showing a relation between the space ($Y$-axis) and time (cumulative day from the first main shock). An arrow indicates the occurrence time of the second main shock (14h38m, May 13, 1997). The dotted line shows the south boundary of the aftershock distribution in Plane-C. Thick lines indicate the no observation periods.

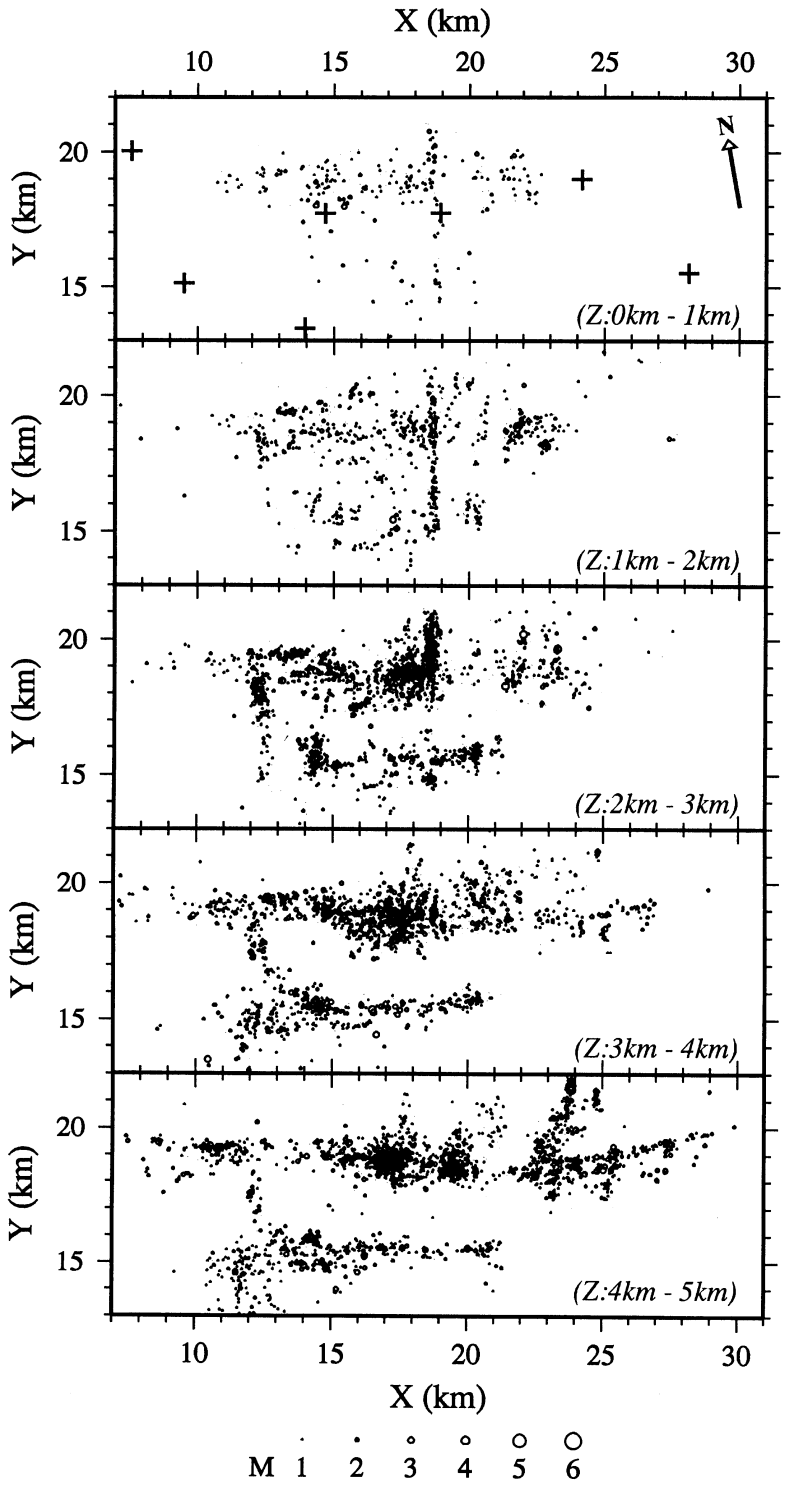


Fig. 9. Aftershock distribution in each layer of 1 km in thickness. Crosses are the station locations.

We tried to estimate the hypocenter of the first main shock (M6.5), which occurred before our temporary observation, with the 3-D model, by collecting 9 aftershocks located by NOEV within a distance of $\pm 1.0$ km from the first main shock location. We compared the hypocenter components with those estimated in the present study and simply evaluated the mean differences: $-0.82$ km, $+0.52$ km and $+0.15$ km for the $X$, $Y$, $Z$ components, respectively. We revised the first main shock location by NOEV, adding these corrections. It is remarkable that a horizontal distance between two main shocks is only 4.8 km.

At first, we describe an outline of the spatial distribution of aftershocks. Most of aftershocks of the first main shock are distributed at depths of 2 to 9 km in the focal region striking nearly E-W (N100°E), which is of 21 km long ($X = 8$ to 29 km) by 3 km wide. It is also found that the first main shock is

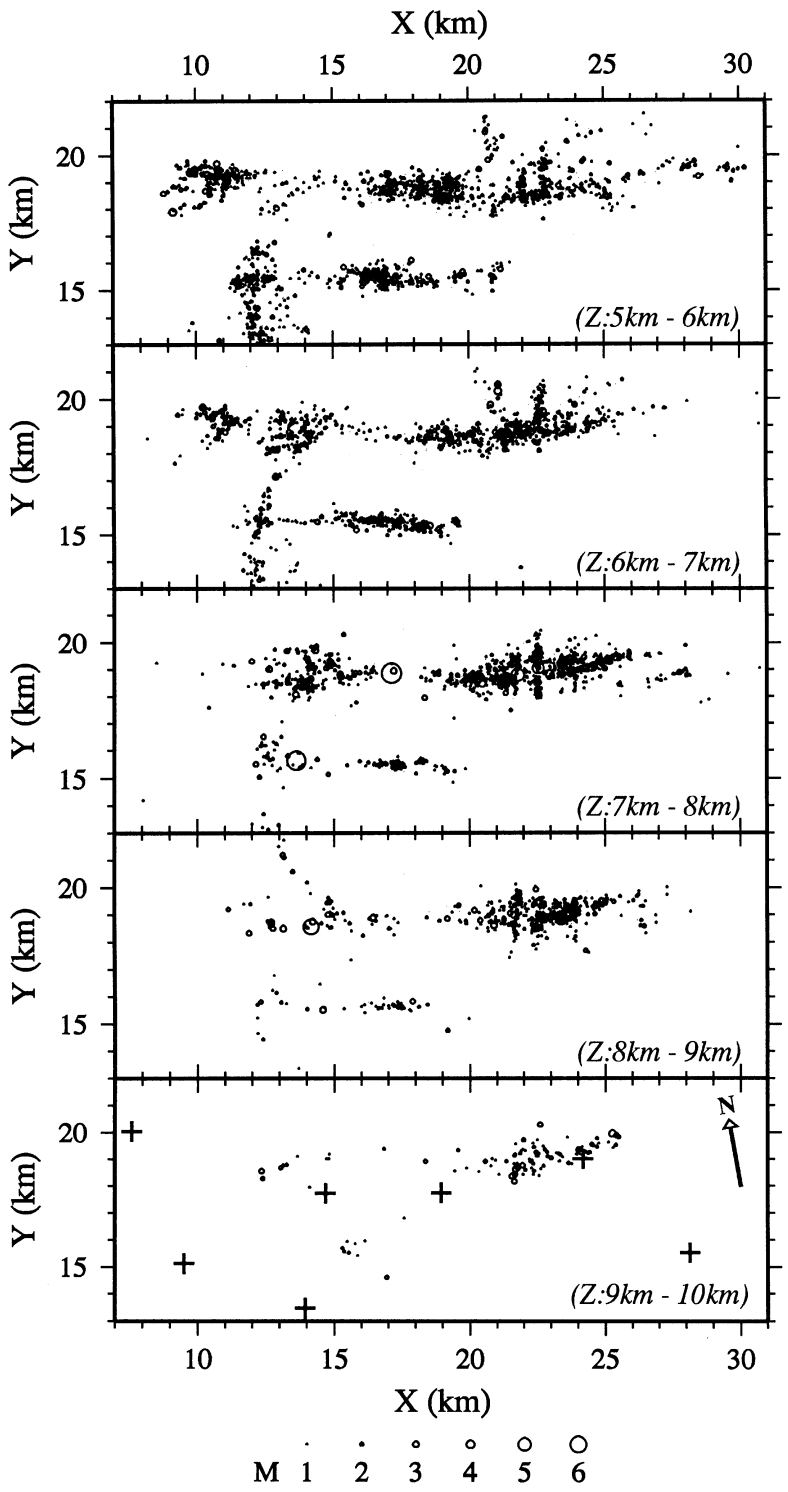


Fig. 9. (continued).

located in the deep middle of the focal region. This suggests that the rupture of the main shock may propagate bilaterally. Hereafter, we call this focal plane as Plane-A. The aftershock distribution for the second main shock is composed of two vertical planes conjugate to each other: one (Plane-B) is a focal region striking nearly E-W (N100°E), parallel to Plane-A, of 11 km long ($X = 10$ to 21 km) by 2 km wide in a depth range from 2 to 9 km, and the other (Plane-C) directed to N-S has an area of 10 km long ($Y = 4$ to 14 km) by less than 2 km wide in a depth range from 4 to 8 km. The second main shock is found to be located not at the intersection of Plane-B and Plane-C, but on Plane-B. It should be also emphasized that Plane-B is clearly separated from Plane-A by a zone like a seismic gap with a horizontal width of 2 to 3 km. As shown in Fig. 5, aftershock activities at the main shock locations are extremely low: aftershocks would presumably be inactive in

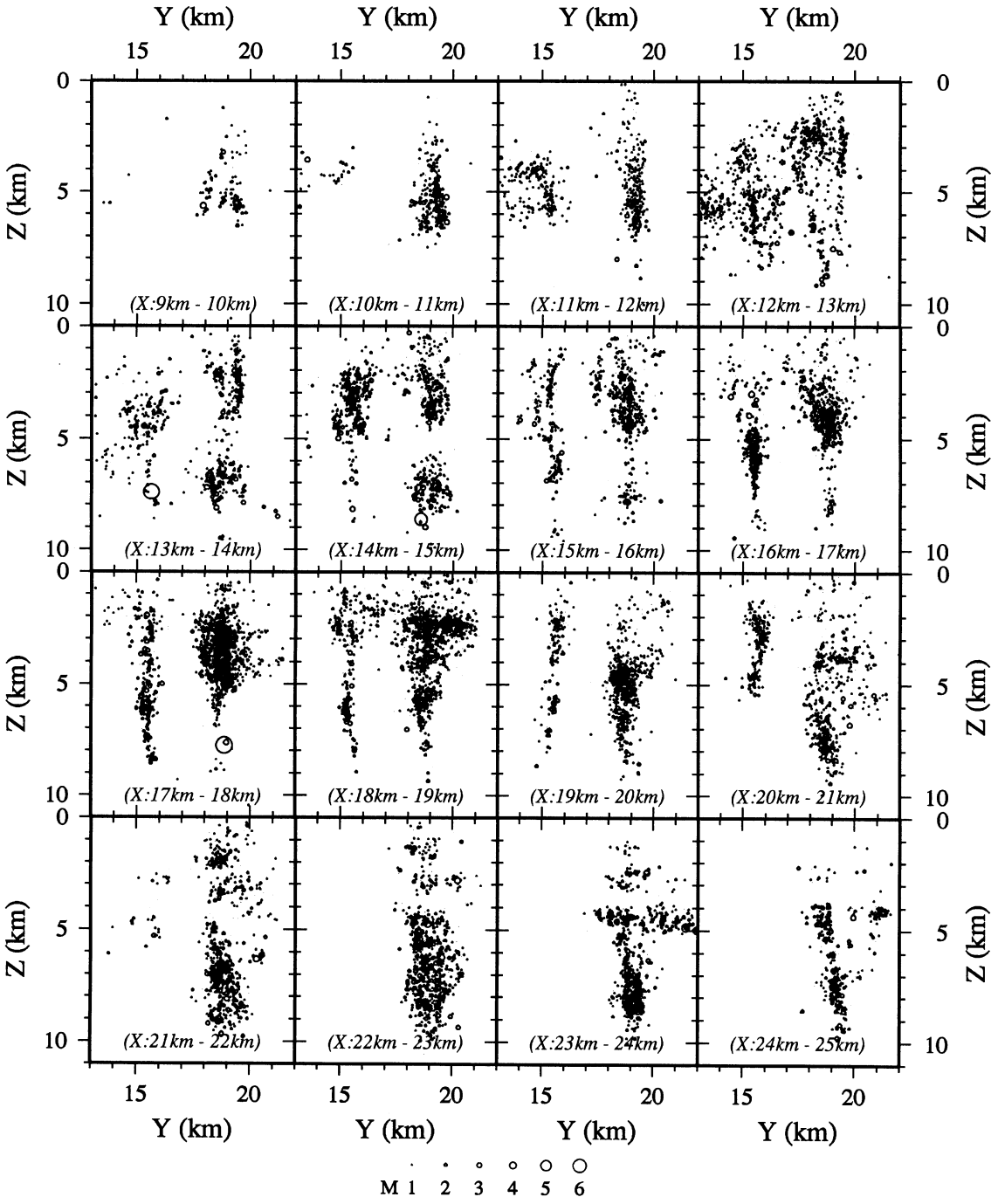


Fig. 10. Vertical cross sections of the aftershocks at an interval of 1 km along the $X$-axis.

a zone highly ruptured by the largest shock. In particular, the zone in Plane-A is found to extend from the main shock location to the western shallow area.

As shown in Fig. 5(c), the aftershocks in Plane-C are found to be restricted in a narrow depth range from 4 to 8 km: those vertically aligned around $Y = 15$ and 19 km correspond to the aftershocks distributed along Plane-A and Plane-B, respectively. We notice that the activity in Plane-C is lower than those in Plane-A and Plane-B during the temporary observation. Figure 8 shows a space-time relation of the aftershocks projected on the $Y$-axis. The aftershock region of Plane-C appears to spread gradually to south: just after the main shock, the horizontal length of Plane-C is less than 5 km and extends up to 10 km at the end of the temporary seismic observation. This southward spread can be seen conspicuously in the aftershock distribution obtained by NOEV (Kakuta *et al.*, 1998). Similarly, Plane-A and Plane-B are about 17 and 9 km long in the early 24 hours from the main shocks, respectively (Kakuta *et al.*, 1998; Miyamachi *et al.*, 1998). Accordingly, we found that each aftershock zone clearly increased its length along its strike. We also see from the figure that the aftershock activity in Plane-A temporally lowered during about three days just after the second main shock.

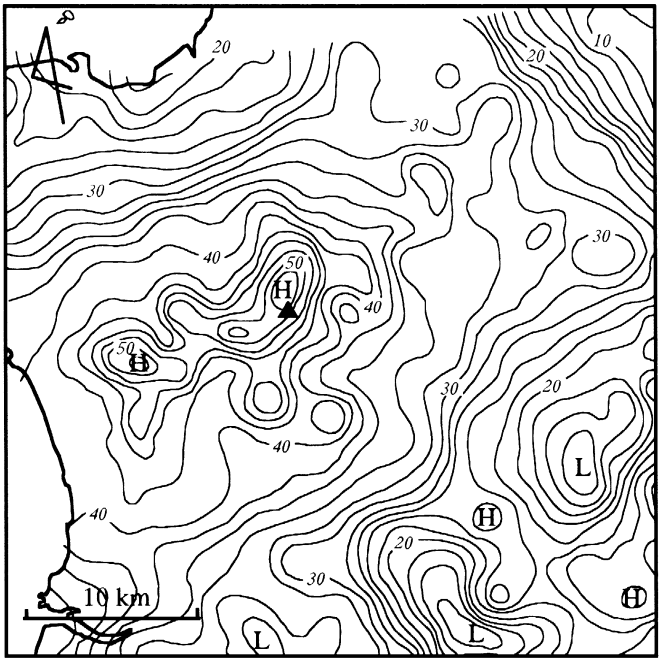


Fig. 11. Bouguer gravity anomalies in the study area (Ministry of International Trade and Industry, 1996). The solid triangle refers to Mt. Shibi.

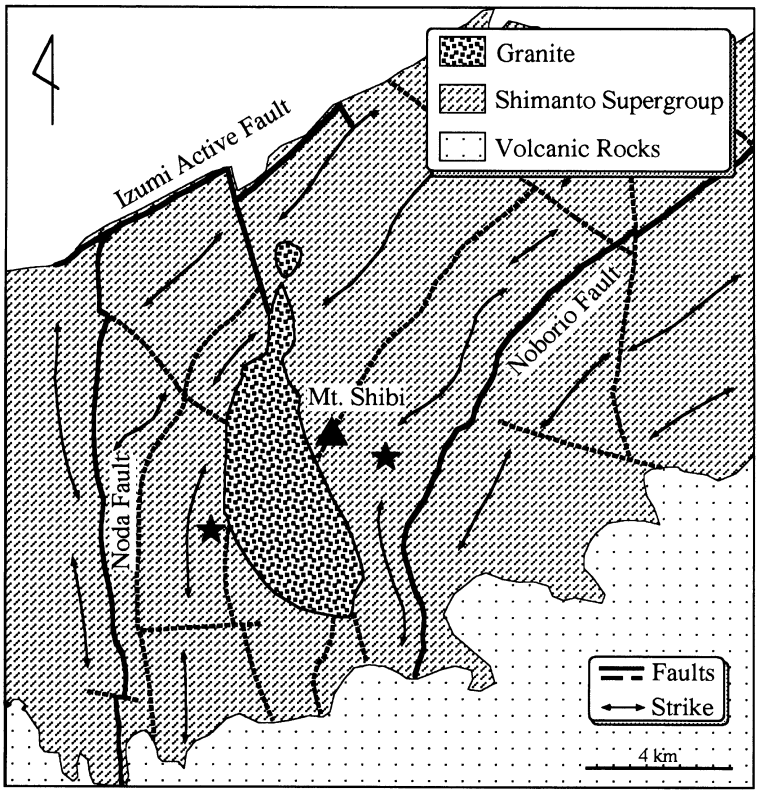


Fig. 12. Geological map simplified from Yoneda and Iwamatsu (1987). Solid stars indicate the locations of two main shocks. The solid triangle corresponds to Mt. Shibi.

A detailed aftershock distribution at each depth interval of 1 km is shown in Fig. 9. Though the aftershocks shallower than 2 km seem to be somewhat scattered, a linear trend of the shallow aftershocks striking nearly N-S at $X = 18$ to 19 km can be seen clearly. In Plane-A, the aftershock distribution at 2 to 4 km depths is complicated. For example, the aftershock zone clearly bends at $X = 15$ km and a linear alignment of the aftershocks trending to N-S is visible at $X = 18$ to 19 km. Aftershocks at $X = 12$ to 13 km at depths of 2 to 5 km seems to extend so as to connect between Plane-A and Plane-B. These aftershocks have occurred just after the first main shock and have been activated after the second main shock. At depths greater than 4 km in the western and middle parts on Plane-A, the aftershock distribution has basically the nearly E-W (N100°E) strike. In the eastern part, however, the major trend of the aftershocks is east. In this part, we observed several N-S alignments of aftershocks, which correspond to the vertical alignments in the deep area at $X = 21$ to 24 km in Fig. 5(a). Most of aftershocks greater than M3.5 occur in the deep area in Plane-A, and especially are concentrated in the eastern part. Figure 10 shows aftershock distributions projected on vertical sections at an interval of 1 km along the $X$-axis. The aftershock distribution on Plane-A is almost vertical in the western and middle parts. However, the plane in the eastern part ($X = 20$ to 25 km) seems to be inclined at about 10 degrees from a vertical. From the section at $X = 23$ to 24 km, we can also see that aftershocks are horizontally distributed in a depth range of 4 to 5 km. The trend of the distribution is found to be almost in a direction of the $Y$-axis from the horizontal section at $Z = 4$ to 5 km in Fig. 9. Plane-B is found to be one straight vertical plane striking nearly E-W (N100°E) in the whole depth range. Moreover, there is no aftershock greater than M3.5. We can see several vertical alignments of aftershocks like a pipe in the shallow area on Plane-B in Fig. 5(b).

## 7. Discussion and Conclusion

Figure 5 shows a close relationship between the velocity structure and the aftershock distribution. Hence, we investigate the relation among the velocity structure, gravity anomaly and geology. We compare the inverted 3-D velocities with the Bouguer anomalies reported by Ministry of International Trade and Industry (1996) shown in Fig. 11. It is evident that the pronounced positive Bouguer anomalies higher than +50 mgal in and around Mt. Shibi are associated with the high velocity zones at depths of 1 and 3 km shown in Fig. 4. Similarly, the low velocity zone east of Mt. Shibi may correspond to the relatively low anomalies of +30 to +40 mgal.

Figure 12 presents a simple surface geological map modified from Yoneda and Iwamatsu (1987). The Cretaceous Shimanto Supergroup, which is composed of alternation of strata of sandstone and mudstone with dip angles from 40°NW to 80°NW, is widely distributed in the study area and is overlain by the Tertiary and Quaternary volcanic rocks in the southeastern part. Its trend changes from NE-SW in the northern part to N-S in the southern part: it is the well-known "Hokusatsu Bend" in geology. The granitic rocks forming Mt. Shibi intruded into the bending zone. It is supposed that the high and low velocity zones in Fig. 4 correspond to the granite and the volcanic rocks covering the Shimanto Supergroup, respectively. Regions of the intermediate velocities may be related to the Shimanto Supergroup. The extent of the high velocity zone beneath Mt. Shibi may suggest that the granitic body is distributed at least down to about 3 km depth. As can be seen in Fig. 12, there is no fault corresponding directly to the aftershock distributions striking nearly E-W, namely Plane-A and Plane-B. However, several N-S oriented lineations seen in the aftershock distributions in Plane-A and Plane-B are almost similar to a trend of the Shimanto Supergroup. On the other hand, the trend of Plane-C is parallel to that of the Shimanto Supergroup and also might be related to Noda Fault striking N-S in the western area. These suggest that these aftershocks may occur along the geological boundaries striking N-S. The surface fault traces caused by two main shocks are not observed (Imura *et al.*, 1998). This fact may be consistent with the upper limit of the main aftershock distribution, 2 km depth.

In the previous section, we pointed out the existence of the vertical alignments of the aftershocks in Plane-A and Plane-B. The horizontal locations of the aftershocks can be generally determined by P wave arrival time data. On the other hand, only P wave data sometimes can not constrain sufficiently the focal depth in the hypocenter determination. Thus, one possible way of verification of the alignments is to inspect the relation between focal depth and S-P time. We select the aftershocks with magnitudes greater than 2 and with various focal depths, located within one alignment ranging from 22 to 23 km in the $X$-axis on Plane-A (see Fig. 5(a)), and show examples of seismograms recorded by the vertical seismometer at HNST which is almost situated above the alignment in Fig. 13. Although it is very hard to detect precisely S wave arrival time on each trace, we can see a tendency that the S-P times increase with focal depth. We think that this auxiliary evidence supports the vertical alignment of the aftershocks. Figure 14 shows a space-time relation of the aftershocks in the alignment selected above. In this alignment, an earthquake with a magnitude of 4.9 occurred on the fourteenth day from the first main shock. Many small aftershocks occurred during a few hours just after this earthquake. Though the aftershocks before the earthquake are spatially concentrated, they are distributed extensively along the $Y$-axis (N10°E) and are mainly located in the shallow region after the earthquake. Similar activity and spatial distribution of aftershocks can be recognized in other vertical alignments. Consequently, it is reasonable to suppose that the relatively big aftershocks may play an important role in the aftershock activities in the vertical alignments and provoke the aftershocks in the alignments to spread to the nearly N-S direction. Further, such alignments of the aftershocks suggest that the aftershocks take place along the underground structural lines, probably geological boundaries or blind faults. Zhao and Negishi (1998) pointed out an important contribution of the fluid-filled, fractured rock matrix to the initiation of the 1995 Kobe Earthquake from their analysis of the distribution of P and S wave velocities and Poisson's ratio in the focal region. We have no information about S wave velocity distribution in this study area. However, because there are many hot springs in the study area, we imagine that the underground fluid or the hydrothermal system, in addition to

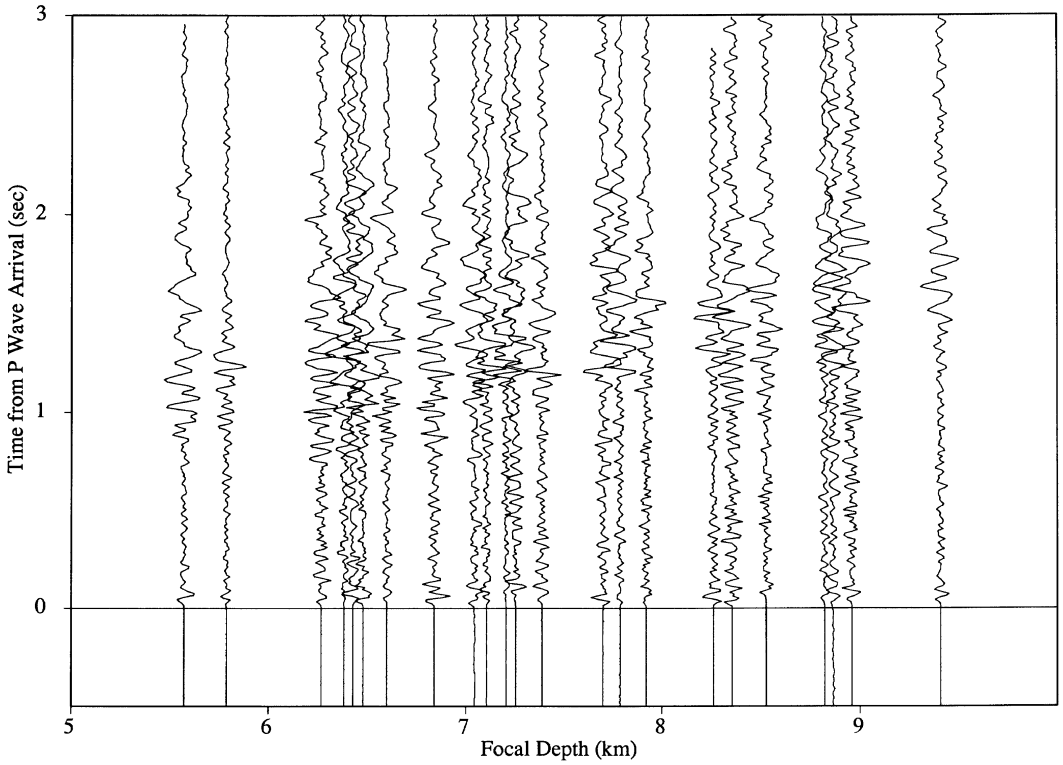


Fig. 13. Seismic waves of the aftershocks located in the vertical alignment in Plane-A with a magnitude greater than 2 recorded by the vertical seismometer at the station HNST. P wave arrival time of each trace is arranged to be 0.0 sec in the axis of ordinate, and the amplitude is normalized by its maximum amplitude.

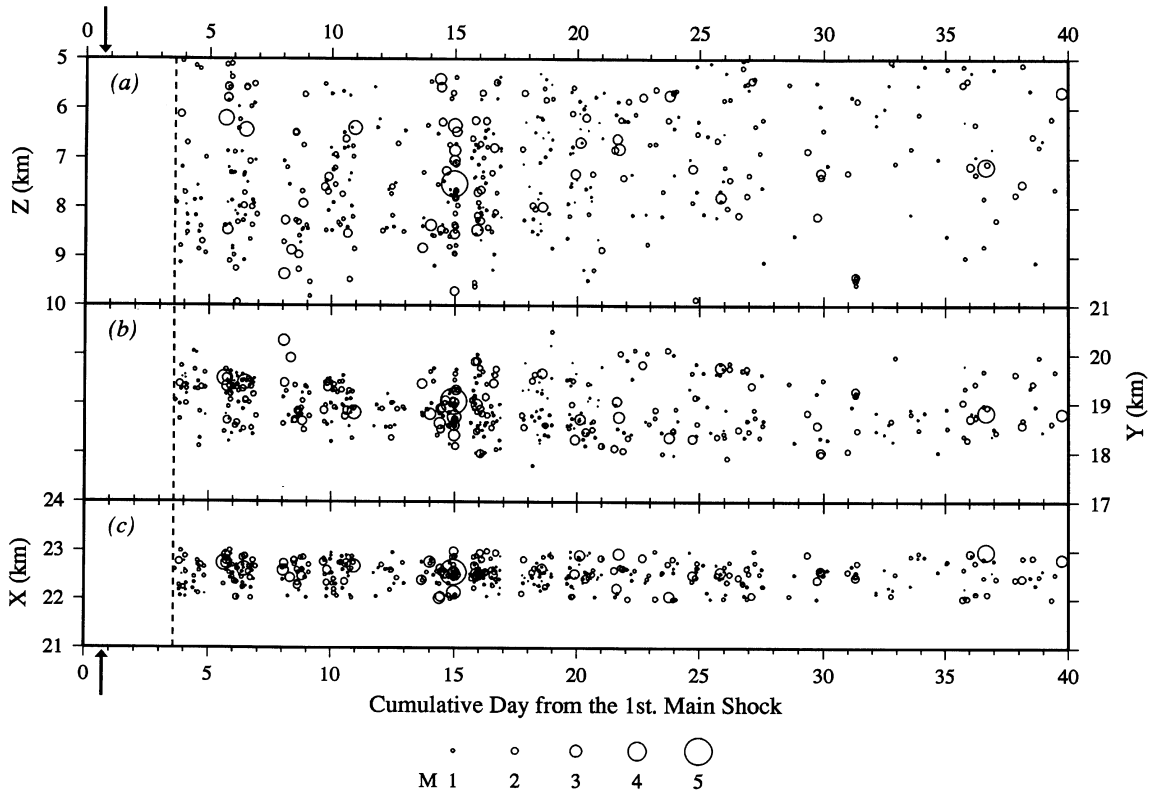


Fig. 14. A time-space relation of the aftershocks located in one vertical alignment on Plane-A: (a) time - $Z$-axis, (b) time - $Y$-axis, and (c) time - $X$-axis. Arrows indicate the time of occurrence of the first main shock. The dotted line shows the beginning of our temporary seismic observation. No observation periods are included in the figure.

the structural boundaries, may participate with the peculiar aftershock distributions.

The 3-D velocity inversion revealed the significant lateral velocity variations in the shallow area. Figure 9 suggests that the spatially complicated distribution of the shallow aftershocks is affected by the underground structure. From Fig. 5, we found that the majority of the aftershocks in Plane-A and Plane-B take place in zones of the intermediate P wave velocities and the aftershock activity is extremely low around the main shocks. Especially, in case of the first main shock, an extremely low aftershock activity zone is clearly found to extend from the hypocenter to the western shallow area. It means that a complete destruction progresses in the zone. We speculate one possible image of the rupture propagation of the first main shocks: (1) the rupture starts at the hypocenter and propagates mainly to west and partly to east, (2) in the western area which is homogeneous from the 3-D velocity model, the rupture will steadily propagate. When its front reaches the shallow high velocity body, the rupture may be disturbed and stops, (3) in the eastern area which seems to be relatively heterogeneous from the model, the rupture immediately reaches the shallow and deep high velocity bodies, and the bodies may prevent the rupture from spreading eastward, (4) as a result, the rupture may concentrate in the intermediate velocity zone, where the most of aftershocks occurred, especially a boundary area between the intermediate and high velocity zones.

In the case of the second main shock, the high velocity body, located in the western shallow area on Plane-B (Fig. 5(b)), may similarly influence the rupture propagation. In the previous section, we mentioned that the second main shock is located not on Plane-C, but certainly on Plane-B. However, as shown in Fig. 8, the aftershocks in Plane-C starts to take place just after the occurrence of the second main shock as well as many aftershocks in Plane-B. Accordingly, it is reasonable to suppose that the rupture starts on Plane-B and will propagate to Plane-C immediately.

The bending axis of the Hokusatsu Bend has not been specified yet in the previous geological studies (Murata, 1987; Yoneda and Iwamatsu, 1987). However, we can presume that the axis has a N100°E-S100°W strike running through near Mt. Shibi, considering the trend of the Shimanto Supergroup. This direction is the same as those of the two aftershock distributions. As pointed out by Imura *et al.* (1998), the main cause of the main shocks may not be the structural movement associated with the Hokusatsu Bend, because the bend had already finished before an intrusion of the granite at Mt. Shibi (Yoneda and Iwamatsu, 1987). On the other hand, from a focal mechanism analysis of the main shocks, Kakuta *et al.* (1998) showed that the $T$-axis is in a NW-SE direction and is almost identical to that of the regional stress field in the study area. If stress concentration had occurred in and around the bending axis, it would have possibly provoked the main shocks to take place near the axis. Consequently, we conclude that the main shocks and their aftershock activity are strongly influenced by the structural complexities in the focal areas.

In future studies, detailed velocity investigations such as conducting artificial explosion experiments with a high density of seismic stations are needed to clarify the relationship between the velocity structure and the main shock and aftershock activity in this area. Moreover, in order to reveal a cause why two big earthquakes, whose horizontal distance is only less than 5 km, occurred successively, an investigation of a dynamic process of the rupture due to the main shocks will be required.

**Acknowledgments.** We would like to express our special appreciation to Mr. S. Hirano (NOEV), and other colleagues for their continuous support to the temporary seismic observation. Most of the figures in this paper are drawn by using the GMT software developed by Wessel and Smith (1991). We are also grateful to the editor Professor T. Tanimoto and two anonymous reviewers for improving the manuscript.

## References

Crosson, R. S., Crustal structure modeling of earthquake data. 1. Simultaneous least squares estimation of hypocenters and velocity parameters, *J. Geophys. Res.*, **81**, 3036–3046, 1976.

Hirahara, K., N. Hirata, A. Ikami, H. Miyamachi, and T. Yabuki, *et al.*, Three-dimensional P and S wave velocity structure in the focal region of the 1984 Western Nagano Prefecture Earthquake, *J. Phys. Earth*, **40**, 343–360, 1992.

Hirata, N. and M. Matsu'ura, Maximum-likelihood estimation of hypocenter with origin time eliminated using nonlinear inversion technique, *Phys. Earth Planet. Inter.*, **47**, 50–61, 1987.

Humphreys, E. and R. W. Clayton, Adaptation of back projection tomography to seismic travel time problems, *J. Geophys. Res.*, **93**, 1073–1085, 1988.

Imura, R., A. Iwamatsu, and K. Kumamoto, Disasters caused by the 1997 earthquakes at northwestern Kagoshima Prefecture, in *General Report on the 1997 Northwestern Kagoshima Prefecture Earthquakes*, 59–69, March, 1998 (in Japanese).

Inoue, H., Y. Fukao, K. Yanabe, and Y. Ogata, Whole mantle P-wave travel time tomography, *Phys. Earth Planet. Inter.*, **59**, 294–328, 1990.

Kakuta, T., H. Miyamachi, K. Goto, H. Yakiwara, S. Hirano, S. Fukumitsu, H. Sekitani, K. Kaneko, K. Iwakiri, and C. Shimizu, Large inland seismic activity in the northern part of Satsuma district, in *General Report on the 1997 Northwestern Kagoshima Prefecture Earthquakes*, 9–20, March, 1998 (in Japanese).

Ministry of International Trade and Industry, Report of regional geological survey; Hokusatsu-Kushikino area, 1995 fiscal year, 1–178, 1996 (in Japanese).

Miyamachi, H. and T. Moriya, Velocity structure and aftershock distribution of the 1982 Urakawa-oki Earthquake, *J. Phys. Earth*, **35**, 309–326, 1987.

Miyamachi, H., K. Iwakiri, T. Tsuno, C. Shimizu, S. Fukumitsu, K. Kaneko, H. Sekitani, T. Kakuta, K. Goto, H. Yakiwara, S. Hirano, T. Matsushima, and H. Shimizu, Temporary seismic observation of aftershocks for the 1977 Northwestern Earthquakes in Kagoshima Prefecture, *Geophys. Bull. Hokkaido Univ.*, **61**, 85–98, 1998 (in Japanese with English abstract).

Murata, A., Hokusatsu bend and clockwise rotation of the southwest Japan arc, *J. Fac. Sci., Univ. Tokyo, Sec. II*, **21**, 333–349, 1987.

Thurber, C. H., Earthquake locations and three-dimensional crustal structure in the Coyote lake area, Central California, *J. Geophys. Res.*, **88**, 8226–8236, 1983.

Um, J. and C. H. Thurber, A fast algorithm for two-point seismic ray tracing, *Bull. Seism. Soc. Am.*, **77**, 972–986, 1987.

Wessel, P. and W. H. F. Smith, Free software helps map and display data, *EOS Trans. Amer. Geophys. U.*, **72**, 441, 445–446, 1991.

Yoneda, S. and A. Iwamatsu, Stratigraphy and geologic structure of the Shimanto super group in the Hokusatsu district, Kagoshima Prefecture, South Kyushu, Japan, *J. Geol. Soc. Japan*, **93**, No. 2, 881–895, 1987 (in Japanese with English abstract).

Zhao, D. and H. Negishi, The 1995 Kobe earthquake: Seismic image of the source zone and its implications for the rupture nucleation, *J. Geophys. Res.*, **103**, 9967–9986, 1998.

H. Miyamachi (e-mail: miya@sci.kagoshima-u.ac.jp), K. Iwakiri, H. Yakiwara, K. Goto, and T. Kakuta